Biosciences

Spectroscopy

A study of acetyl-CoA decarbonylase/Synthase using x-ray magnetic circular dichroism at beam line 4.02 of the ALS
Funk, T., S. Friedrich, W. Gu, D.A. Grahame, S.P. Cramer

Absolute flux measurements for IR spectromicroscopy
Martin, M.C., K. Knutsen, W.R. McKinney

Catalysis of PAH biodegradation by humic acid shown in synchtrotron infrared studies
Holman, H.-Y., K. Nieman, D.L. Sorensen, C.D. Miller, M.C. Martin, T. Borch, W.R. McKinney, R.C. Sims

FTIR spectroscopy of bacteriorhodopsin microcrystals at Beamline 1.4
Betancourt, F., S. Rouhani, M. Facciotti, F. Burkard, R. Glaeser

Hard tissue ablation and modification with IR lasers
Fried, D., T. Breunig

Investigation of calcifications in breast tissue using EXAFS and XRF
Sayers, D.E., M.Z. Kiss, A.C. Thompson, M. Marcus

Novel molecular mechanisms of disease susceptibility in plants—an FTIR study of *Arabidopsis thaliana*
Raab, T.K., J. Vogel, S. Somerville

Osteoblast-like cell adhesion on bioactive glasses: Surface reactions and resistance to trypsinization
Foppiano, S., A.P. Tomsia, G.W. Marshall, T. Breunig, D.J. Rowe, S.J. Marshall

Synchrotron infrared spectromicroscopy as a novel bioanalytical microprobe for individual living cells: Cytotoxicity considerations
Holman, H.-Y., K.A. Bjornstad, M.P. McNamara, M.C. Martin, W.R. McKinney, E.A. Blakely

A Study of Acetyl-CoA Decarbonylase/Synthase Using X-Ray Magnetic Circular Dichroism at Beam Line 4.02 of the ALS

T. Funk[1], S. Friedrich[1], W. Gu[2], D.A. Grahame[3] and S. P. Cramer[1,2]

[1]Lawrence Berkeley National Lab, Cyclotron Road 1, Berkeley, CA 94720 USA
[2]Department of Applied Science, UC Davis, One Shields Avenue, Davis, CA 95616 USA
[3]Dept. of Biochemistry and Molecular Biology, USUHS, 4301 Jones Bridge Road, Bethesda, MD 20814 USA

INTRODUCTION

X-ray magnetic circular dichroism (XMCD) spectroscopy provides a unique opportunity to study spin and oxidation states of dilute transition metals in metallo proteins. Advantages of the technique include element selectivity and high sensitivity.
The XMCD signal is given by the difference in absorption between right and left circular polarized X-rays [1]. XMCD probes the population of the magnetically split levels by measuring the difference in absorption between right and left circular polarized X-rays. Since in paramagnetic systems this population is given by Boltzmann statistics, XMCD requires high fields and low temperatures.
Applying the sum rules to the measured spectra allows determining the spin and the orbital angular momentum of the metal centers [2]. Furthermore, one can observe the signal as function of the magnetic field to get magnetization curves of the system. This allows to extract the total angular momentum and the g-factor of the specific metal sites by fitting a Brillouin function. This also provides information, if various chemical species of the same element are present.
We have studied the active site of the enzyme acetyl-CoA decarbonylase/synthase (ACDS) using this method. ACDS contains 5 protein subunits and catalyzes the cleavage (or synthesis) of acetyl-CoA [5]. In the current model, the active site A cluster (which is located on the ACDS β subunit) contains an Fe-S cluster with a Ni atom bridged to it [3]. During the catalytic cycle of ACDS the Ni and the Fe sites change the oxidation state. An important step to understand the catalyzes is to understand the various steps in the catalytic cycle.

EXPERIMENTS

With our current setup located at the elliptically polarized undulator beam line of the ALS we can study systems with a metal concentration of 500 ppm and below utilizing a commercial 30 element Ge detector. Our endstation hosts a 6 Tesla superconducting magnet cooled with liquid helium. The sample is located in the bore of the magnet and is attached to a separate pumped ^{4}He cryostat providing sample temperatures of 2.2 K [4].
The proteins are prepared in a dried film on a sapphire disk in a glove box. The sample is transferred to the experimental chamber and cooled to base temperature in a specially designed capped sample holder.
We prepared ACDS β sununit in 2 states important for the catalyzes. One state was obtained by reducing the protein with Ti citrate and another was obtained treating the reduced protein with CO.
The magnetic response was studied at the Ni and the Fe sites recording the respective L-edges with circularly polarized light at 2.2K and 6T.

RESULTS AND DISCUSSION

Ti citrate reduced ACDSβ shows a strong magnetic signal in the Ni as well as in the Fe spectrum.
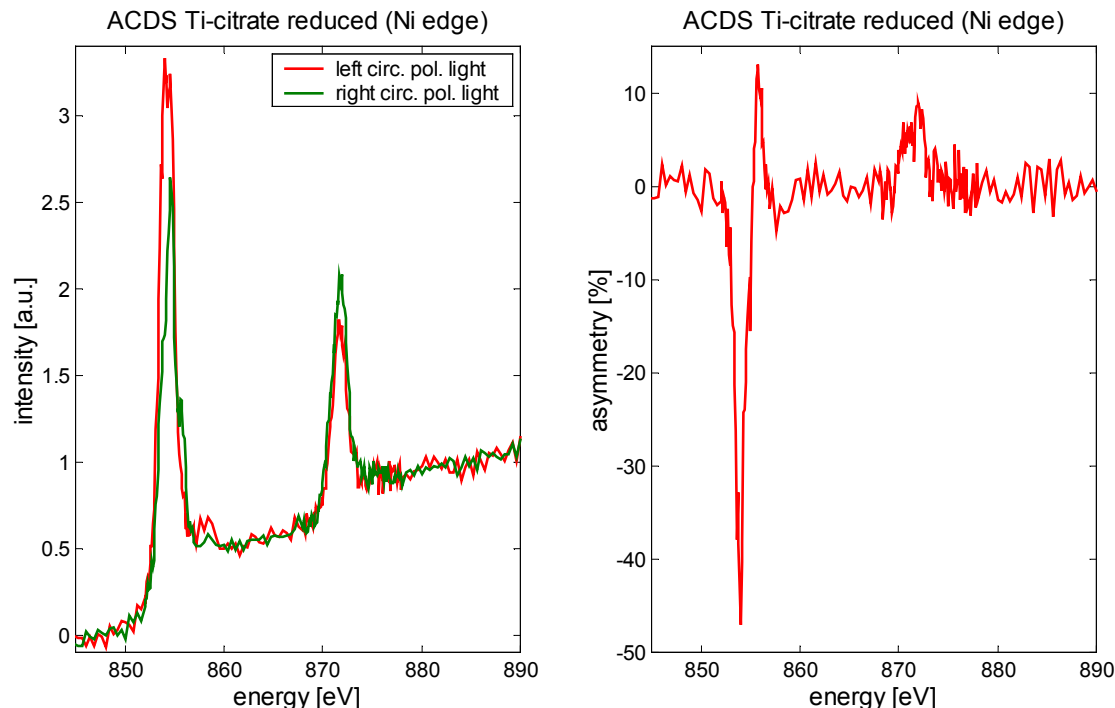

Figure 1a and 1b: L-edge spectra with right and left circularly polarized light (a). Difference of with right and left circularly polarized light spectra and normalized to maximum of L-edge spectrum (b).
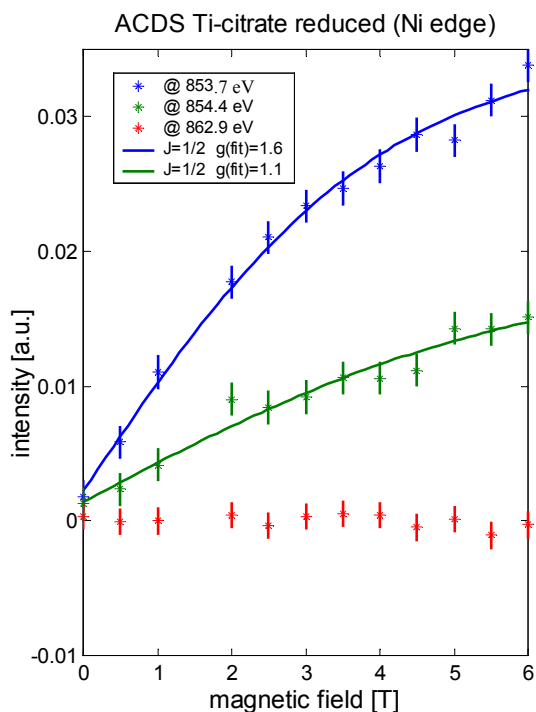

Figure 2: Magnetization curves at different excitation energies. The red curve was taken between the L3 and L2 line and shows no signal

Figure 1a shows the L-edge spectra of Ni for left and right circularly polarized light. Figure 1b shows the XMCD signal taking the difference spectrum between left and right circularly polarized light normalized with the maximum of the L-edge spectra leading to an XMCD effect of around 50%. Magnetization curves were taken at various excitation energies as shown in figure 2. One curve was measured at 862.9 eV just between the L3 and L2 lines. Since no magnetic response is expected at this position this curve determines the base line. Another set of curves were taken at two positions of the L3 line. Fits of the Brillouin function to the data results in different g-values. This indicates the presence of different chemical species of Ni in the sample with different magnetic properties. The measured spectrum is a superposition of the spectra of the different species. A similar behavior was observed for the magnetization curves taken at the Fe edge. The L3 edge is

showing a double peak feature with both peaks exhibiting a strong magnetic response. The maximum XMCD signal is about 35%.

Treating the sample with CO changes the resulting spectra dramatically. The magnetic signal on the Ni site disappears almost completely. A residual XMCD signal of 10% is observed. Also the XMCD signal of the Fe is drastically reduced to about 20%. The double peak feature at the L3 line also disappears. A magnetization curve was taken at the excitation energy of the maximum Fe-XMCD signal revealing a magnetization close to saturation. This rules out that the XMCD signal disappeared due to insufficient thermal contact.

ACKNOWLEDGEMENTS

REFERENCES

[1] J. Stöhr and Y. Wu in: New Directions in Research with Third-Generation Soft X-Ray Synchrotron Radiation Sources, Eds. A.S. Schlachter and F. J. Wuilleumier, Kluwer Academic Publishers (1994), 221
[2] S. Cramer *et al.,* ACS symposium series 692, **154** (1997)
[3] S. W. Ragsdale, and M. Kumar, *Chem. Rev.* **96**, 2515 (1996)
[4] T. Funk, S. Friedrich, A. Young, E. Arenholz and S. P. Cramer, RSI **73,3** (2002)
[5] B. Bhaskar, E. DeMoll, and D.A. Grahame, *Biochemistry* **37,** 14491-14499 (1998)

Principal investigator: Stephen P. Cramer, Department of Applied Science, UC Davis, and Ernest Orlando Lawrence Berkeley National Laboratory. E-mail: cramer@lbl.gov, telephone: 510-486-4720.

Absolute Flux Measurements for IR Spectromicroscopy

Michael C. Martin[a], Kelly Knutsen[b] Wayne R. McKinney[a]

[a] Advanced Light Source Division, Lawrence Berkeley National Laboratory, Berkeley, CA 94720
[b] Dept. of Chemistry, University of California, Berkeley, CA 94720

1. INTRODUCTION

Measurements of the effects of exposure to IR light at the spectromicroscope at beamline 1.4.3 has necessitated an estimate of the absolute flux levels in the IR optical bench and in the microscope. We calculated the IR flux levels from both a thermal source and the ALS, and compared them to measurements taken at the beamline. We find a self consistent picture which can be used to estimate the absolute exposure to cells and bacteria which are examined in the IR microscope.

2. EXPERIMENTAL

The thermal ("globar") source in the Nicolet 760 IR bench was measured with a disappearing filament style optical pyrometer to have a brightness temperature of ~1343K. This allowed us to calculate the "greybody power" emitted by the filament, using the emissivity of tungsten. We also measured the output of the thermal source with a Molectron PowerMax 500D with a 19 mm dia. PM10V1 detector. To measure ratios of light both before and after the bench and the microscope a more sensitive mid IR detector was needed so we employed a T3-09 9mm dia. energy detector, and a 200 Hz chopper. We also calculated the power of the synchrotron beam using the standard bending magnet formulae. The table below summarizes our results. Unless enumerated otherwise the numbers are in watts. Bold numbers are experimental data, others are calculations or estimates.

Greybody power 1 to 20 microns 1 mm^2, 0.0064 str, 1343 K	1.70E-04	**0.0479**	Synchrotron Power 1 to 20 microns 10 x 40 mr, 1.9 GeV, 4.81 m	3.73E-02
Real emitting area, mm^2	100	1	Beamline coupling loss 20 out of 40 mr * 0.67 diamond	0.333
Bench efficiency Chopped Energy Detector **15.9/42.7**	0.372	0.372	Bench efficiency Chopped Energy Detector **15.9/42.7**	0.372
Microscope Vignetting Chopped Energy Detector **1.5/15.9 * 12^2/9^2**	0.1677	0.1677	Microscope Vignetting	1
Microscope efficiency **0.6/(1.5*12^2/9^2)** Chopped Energy Detector	0.225	0.225	Microscope efficiency **0.6/(1.5*12^2/9^2)** Chopped Energy Detector	0.225
Power at sample Greybody	2.39E-04	6.72E-04	Power at Sample Synchrotron	1.04E-03
Ratio of Synch/Greybody by MCT in Microscope		**2**	Peak Power at Sample Synchrotron (*50)	5.20E-02
Ratio from this work	1.55		for 2ns/40ps	

3. RESULTS AND DISCUSSION

Starting from two calculations, and one measurement the table precedes from top to bottom from the two sources, thermal and synchrotron to the sample. At each step, there were many factors to consider. For example, the long depth of field of the synchrotron source means that all 40 horizontal mr of beam is not coupled into the microscope, and the synchrotron beam has a diamond window loss which the thermal beam does not. Moreover, the synchrotron beam has been carefully moved from the center of the optical axis so that it is not vignetted by the special coating in the center of the beam splitter in the optical bench, and the microscope optics have been adjusted to optimally transmit the synchrotron beam. This requires that the vignetting ratios for the two cases be different. We have done our best to honestly estimate the various factors, and measure them where feasible without significant disassembly of the beamline optics.

The final results are satisfying in that the ratio of the total synchrotron to thermal flux (1.55) that we get from our careful combination of theoretical and experimental measurements matches well within the error of our methods the ratio (2.0) we measure by comparing the two sources directly with the LN_2-cooled MCT detector in the microscope. The brightness advantage of the synchrotron (>100) is also verified. The overall error in the estimates is well represented by the factor of 2.8 between the two methods for estimating the power of the thermal source. The continuous power at the microscope integrated from 400 to 10000 cm^{-1} is estimated to be approximately 1 mW, and the peak power at the top of an ALS pulse to be fifty times (2 nsec / 40 psec) that, or 50 mW.

REFERENCES

1. Michael C. Martin, Nelly M. Tsvetkova, John H. Crowe, and Wayne R. McKinney, "Negligible sample heating from synchrotron infrared beam," Applied Spectroscopy, **55**(2), 111-113 (2001).

2. Hoi-Ying N. Holman, Michael C. Martin, Eleanor A. Blakely, Kathy Bjornstad, and Wayne R. McKinney, "IR spectroscopic characteristics of cell cycle and cell death probed by synchrotron radiation based Fourier transform IR spectromicroscopy," Biopolymers (Biospectroscopy), **57**[6], 329-335 (2000).

3. Hoi-Ying N. Holman, Kathleen A. Bjornstad, Morgan P. McNamara, Michael C. Martin, Wayne R. McKinney, and Eleanor A. Blakely, "Synchrotron Infrared Spectromicroscopy as a Novel Bioanalytical Microprobe for Individual Living Cells: Cytotoxicity Considerations," Journal of Biomedical Optics 2002, *In Press.*

Principal investigator: Michael C. Martin, Advanced Light Source Division, LBNL, 510-495-2231, MCMartin@lbl.gov

Catalysis of PAH Biodegradation by Humic Acid Shown in Synchrotron Infrared Studies

Hoi-Ying N. Holman,[1] Karl Nieman,[2] Darwin L. Sorensen,[2] Charles D. Miller,[3]
Michael C. Martin,[4] Thomas Borch,[5] Wayne R. McKinney,[4] and Ronald C. Sims[2]

[1]Center for Environmental Biotechnology, Lawrence Berkeley National Laboratory, Berkeley, CA 94720
[2]Utah Water Research Laboratory, Utah State University, Logan, UT 84321
[3]Biology Department, Utah State University, Logan, UT 84321
[4]Advanced Light Source Division, Lawrence Berkeley National Laboratory, Berkeley, CA 94720
[5]Center for Biofilm Engineering, Montana State University, Bozeman, MT 59717

INTRODUCTION

Humic acids (HAs) are complex organic molecules produced by the decomposition of plant and animal remains in soils. The surfactant-like micellar microstructure of HA is thought to accelerate the degradation of polycyclic aromatic hydrocarbons (PAHs) by enhancing PAH solubility, thereby increasing the PAH bioavailability to microorganisms. Despite abundant evidence that HA is important in the bioremediation of several anthropogenic pollutants, its role in the detoxification of PAHs by microbes remains uncertain.

Previous inconclusive results motivate a novel approach to the study of this important biogeochemical process. We used SR-FTIR spectromicroscopy to examine the effects of soil HA on biodegradation of the model PAH pyrene in the presence of a colony of Mycobacterium sp. JLS, on a mineral surface in an unsaturated environment. Infrared spectra measured during the onset and progress of biodegradation constitute the first microscopic study of this process to be made in real time.

PROCEDURE

SR-FTIR spectra were obtained at ALS BL1.4.3 from samples of M. sp. JLS as they degraded pyrene on magnetite surfaces, with and without the addition of Elliott Soil Humic Acid (ESHA). The pyrene-degrading microorganism M. sp. JLS is a gram-positive, rod-shape bacterium (GenBank accession no. AF387804); our samples were recently isolated from PAH-contaminated soil at the Libby Groundwater Superfund Site in Libby, Montana, USA. Our mineral substrates were freshly cleaved and sonicated surfaces of small chips (less than 1 cm in diameter) of magnetite rock from Minerals Unlimited of Ridgecrest, CA.

The time-dependent pyrene biodegradation experiments were began by adding 2.5 ml of cell suspension (~1.5 × 108 cells/milliliter) of M. sp. JLS onto the prepared magnetite chips. A custom IR microscope-stage mini-incubator was used to maintain the proper growth conditions for M. sp. JLS, while allowing *in situ* FTIR spectromicroscopy measurements. For abiotic controls, no M. sp. JLS was applied. Non-overlapping IR spectral markers were selected to monitor each component.

RESULTS

Figure 1 summarizes the time series of infrared spectra obtained by repeatedly measuring the same location on each pyrene-coated sample for more than a month. Since the sample surface is different for each experiment, the absolute value of absorbance can vary. However by
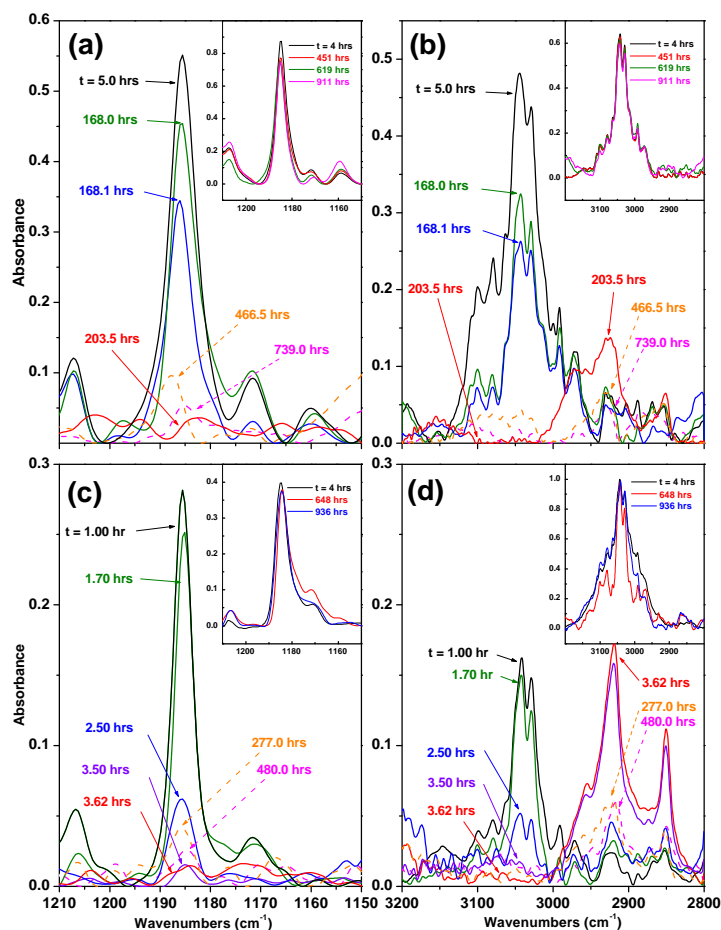
Figure 1. Time series of SR-FTIR absorption bands corresponding to pyrene and biomass formation following the degradation of pyrene by Mycobacterium sp. JLS on magnetite surfaces. Panels (a) and (b) are without ESHA; panels (c) and (d) are with ESHA. (a) and (c) show a pyrene absorption band at 1185 cm^{-1}. (b) and (d) show a pyrene doublet at 3044 and 3027 cm^{-1} and biomass IR absorption at 2921 and 2850 cm^{-1}. Inserts are abiotic control experiments.

monitoring the same position on each sample individually, the changes in absorption are quantitative. Over a similar period, the infrared spectra obtained from samples free of pyrene did not show statistically significant changes.

For samples without ESHA, pyrene biodegradation starts very slowly, and about 168 hours elapse before significant changes are observed. Biodegradation then proceeds quickly, and all the observed pyrene is completely degraded within the next 35 hours. As the pyrene peaks in the spectra disappear, we observe an increase in the biomass IR absorption peaks, implying concurrent biomass formation during the consumption of pyrene (Fig. 1, panels (a) and (b)). By contrast, the biodegradation of pyrene on samples with ESHA begins almost immediately (~1 hour) after the introduction of M. sp. JLS (Fig. 1, panels (c) and (d)). The degradation of the observed pyrene is complete by the fourth hour. Again we detect an increase in biomass absorption during the later stage of the pyrene degradation, which implies that biomass formation is concurrent with the consumption of pyrene.

Figure 2 displays pyrene concentration and biomass versus time under three different conditions, as measured by associated spectral absorbances normalized to remove surface effects as described above. Abiotic results show that pyrene remains on the mineral surface, with only slow removal mechanisms. Pyrene degradation by M. sp. JLS without ESHA did not proceed until ~ 170 hours after the introduction of the bacteria, followed by a rapid decrease of pyrene and a rapid increase of biomass within the next thirty-five hours, as described earlier. After the pyrene was depleted the biomass signal significantly decreased, presumably as the M. sp. JLS bacteria transformed themselves into ultramicrocells, a starvation-survival strategy commonly observed among bacteria in oligotrophic environments. In the presence of ESHA, pyrene biodegradation begins within an hour and the observed pyrene is depleted by the end of the fourth hour, with a concurrent increase of biomass. It is likely that the water-insoluble pyrene is solubilized into cores of ESHA pseudo-micelles and therefore becomes available for bacterial consumption.

Over longer times, IR absorption bands of pyrene on magnetite surfaces showed a slight increase and decrease. The increase is probably due to pyrene diffusing from pyrene trapped in
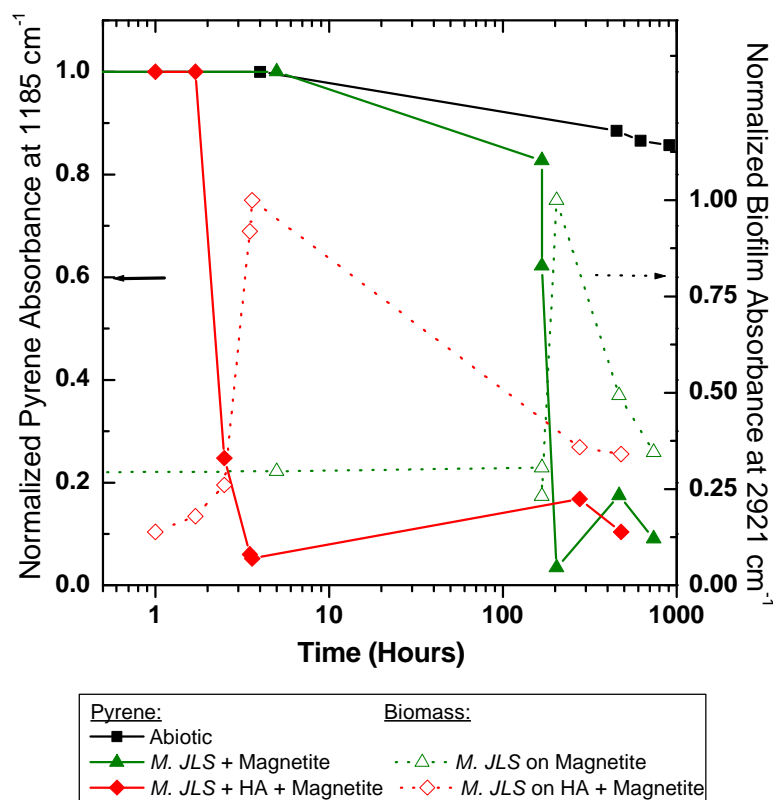
Figure 2. Summary of IR results showing that pyrene degradation occurs much faster when ESHA is present (note the log scale on the time axis). The color scheme is black for abiotic, green for biotic without ESHA, and red for biotic with ESHA. The solid lines correspond to pyrene and the dotted lines correspond to the biomass.

micropores of the magnetite and/or neighboring surfaces of higher pyrene concentration. Thus the first wave of rapid depletion of pyrene by M. sp. JLS set up a diffusion gradient from the pyrene-containing micropores toward the bacterial colony, leading to a subsequent small increase in pyrene concentration. For the surface containing ESHA, the biomass remained almost constant over a period of more than 200 hours, indicating that the flux of pyrene from the micropores was sufficient to maintain the bacterial colony. For the surface free of ESHA, there is little evidence of the presence of a quasi-steady state biomass.

DISCUSSION

Our results have significant implications for the bioremediation of contaminated soils. In many PAH-contaminated sites, bioremediation is specified by the U.S. Environmental Protection Agency as the preferred remedial technology. Bioremediation of PAH-contaminated soils is often limited, however, by the low solubility of PAH, which inhibits microbial uptake. Adding synthetic surfactants to enhance PAH solubility may be toxic to natural microorganisms and further inhibit bioremediation. Based on results reported here, a potential alternative in unsaturated soil environments may be the application of natural HA to accelerate the biodegradation of PAH.

SR-FTIR spectromicroscopy can assess real-time interactions between multiple constituents in contaminated soils. Combined with conventional mineralization measurements, which monitor respiration through carbon dioxide production, SR-FTIR spectromicroscopy is a powerful tool for evaluating bioremediation options and designing bioremediation strategies for contaminated vadose zone environments.

FTIR spectroscopy of bacteriorhodopsin microcrystals at Beamline 1.4

F. Betancourt[1], S. Rouhani[2], Marc Facciotti[3], F. Burkard[1], and R. Glaeser[1,2,3]

[1]Life Sciences Division, Ernest Orlando Lawrence Berkeley National Laboratory,
University of California, Berkeley, California 94720, USA
[2]Department of Molecular and Cell Biology, University of California, Berkeley, California 94720, USA
[3]Biophysics Group, University of California, Berkeley, California 94720, USA

Bacteriorhodopsin (bR) is the sole protein component of the purple membrane of *Halobacterium salinarium* [1]. The function of bR *in vivo* is to convert solar energy into a pH gradient across the cell membrane which the organism uses to drive ATP synthesis [2]. Bacteriorhodopsin undergoes a light-induced cycle of physicochemical changes for for every proton it pumps out of the cell. The photocycle of bR has been well-characterized by both visible and IR spectroscopy. The major intermediates are identified as the K, L, M, N and O intermediates, and each has a distinct visible color and a distinct IR spectrum [3]. The Schiff base that connects the side chain of Lys 216 to the retinal molecule buried within the core of the apoprotein [4] is deprotonated upon formation of the M intermediate, and reprotonated when the M intermediate decays. Since access to the Schiff base switches from the extracellular side of the membrane to the cytoplasmic side between these two proton transfer events, the M intermediate is of particular interest.

High resolution x-ray diffraction experiments on microcrystals of bR have recently become possible, through the discovery by Landau and Rosenbusch that the solubilized protein can be crystallized from the bicontinuous lipid-water gel that is formed by mono-olein [5]. Structural studies on intermediate states of the photocycle thus become a high priority, allowing the visualization of the structural changes that are responsible for converting light energy into a proton-motive force.

Previously we collected high resolution x-ray diffraction data from crystals of wild type bR trapped in both the L and M states by illumination at low temperature, using Fourier Transform IR (FTIR) spectroscopy to confirm the identity of the photointermediate[6]. This year we turned our attention this year to the F219L mutant of bR, which forms N, the intermediate following M, more readily than does the wild type protein[7]. We have succeeded in characterizing two photointermediates of the bacteriorhodopsin mutant F219L by means of FTIR spectroscopy. At 213K an early phase of the M photostate is trapped, whereas at 173K the IR signature strongly suggests that the L photostate is trapped. Further studies of this mutant are planned, with an eye towards trapping the N intermediate.

REFERENCES

1. Oesterhelt, D. & Stoeckenius, W. Rhodopsin-like protein from the purple membrane of Halobacterium halobium. *Nature New Biology* **233**, 149-152 (1971).
2. Racker, E. & Stoeckenius, W. Reconstitution of purple membrane vesicles catalyzing light-driven proton uptake and adenosine triphosphate formation. *Journal of Biological Chemistry* **249**, 662-663 (1974).
3. Lozier, R. H., Bogomolni, R. A. & Stoeckenius, W. Bacteriorhodopsin: a light-driven proton pump in *Halobacterium halobium. Biophysical Journal* **15**, 955-962 (1975).
4. Henderson, R. et al. Model for the structure of bacteriorhodopsin based on high-resolution electron cyro-microscopy. *Journal of Molecular Biology* **213**, 899-929 (1990).
5. Landau, E. M. & Rosenbusch, J. P. Lipidic cubic phases: A novel concept for the crystallization of membrane proteins. *Proceedings of the National Academy of Sciences USA* **93**, 14532-14535 (1996).
6. Facciotti, M. T. et al. Structure of an early intermediate in the M-state phase of the bacteriorhodopsin photocycle. *Biophysical Journal* **81**, 3442-3455 (2001).
7. Vonck, J. A three-dimensional difference map of the N intermediate in the bacteriorhodopsin photocycle: Part of the F helix tilts in the M to N transition. *Biochemistry* **35**, 5870-5878 (1996).

Principal investigator: Felicia Betancourt, Advanced Light Source, Lawrence Berkeley National Laboratory. Email: fmh@xtalu.lbl.gov. Telephone: 510-486-6597.

Hard Tissue Ablation and Modification with IR Lasers

D. Fried and T. Breunig,

Department of Preventive and Restorative Dental Sciences, 707 Parnassus Ave. University of California
San Francisco, 94143-0758

Infrared lasers are ideally suited for the selective and precise removal of carious dental hard tissue while minimizing the healthy tissue loss. Since the initial investigations of Stern[1] over 30 years ago, several unique laser applications have evolved for dentistry, namely laser ablation of dental hard tissue, caries inhibition treatments by localized surface heating, and surface conditioning for bonding[2]. During high intensity laser irradiation, marked chemical and physical changes may be induced in the irradiated dental enamel. These changes can have profound effects on the laser ablation/drilling process and may lead to a reduction in the ablation rate and efficiency, increase peripheral thermal damage and even lead to stalling without further removal of tissue with subsequent laser pulses. Moreover, thermal decomposition of the mineral can lead to changes in the susceptibility of the modified mineral to organic acids in the oral environment. Morphological changes may result in the formation of loosely attached layers of modified enamel that can delaminate leading to failure during the bonding to restorative materials [3, 4]. Therefore, it is important to thoroughly characterize the laser (thermal) induced chemical and crystalline changes after laser irradiation. The mineral, hydroxyapatite, found in bone and teeth contains carbonate inclusions that render it highly susceptible to acid dissolution by organic acids generated from bacteria in dental plaque. Upon heating to temperatures in excess of 400 °C, the mineral decomposes to form a new mineral phase that has increased resistance to acid dissolution[5]. Recent studies suggest that as a side effect of laser ablation, the walls around the periphery of a cavity preparation will be transformed through laser heating into a more acid resistant phase with an enhanced resistance to future decay[6]. However, poorly crystalline non-apatite phases of calcium phosphate may have an opposite effect on plaque acid resistance[7] and may increase the quantity of poorly attached grains associated with delamination failures.IR spectroscopy has been used for half a century to study the structure of bony tissue[8, 9]. Fowler and Kuroda [7, 10] used IR transmission spectroscopy to show the chemical changes induced in laser irradiated dental enamel. Recently, we demonstrated that FTIR in specular reflectance mode could be used effectively to nondestructively measure the laser-induced chemical changes in enamel and that the carbonate loss could be determined as a function of incident laser intensity[11]. However, this technique requires smooth surfaces of large area in order to acquire suitable spectra. The high brightness of the ALS enables spectra to be acquired on specific areas across ablation craters with a resolution of 10 μm.

FTIR spectroscopy was used in the specular reflectance mode for resolving thermally induced changes in dental hard tissue as a result of laser irradiation. High spatial resolution (10 μm) was used with the high brightness available on beam line 1.4.3 for these studies. IR spectra of modified bovine enamel were acquired after laser ablation using several laser wavelengths from the UV to the mid-IR. Specific areas within the laser-ablated region were examined to determine the structural and chemical composition
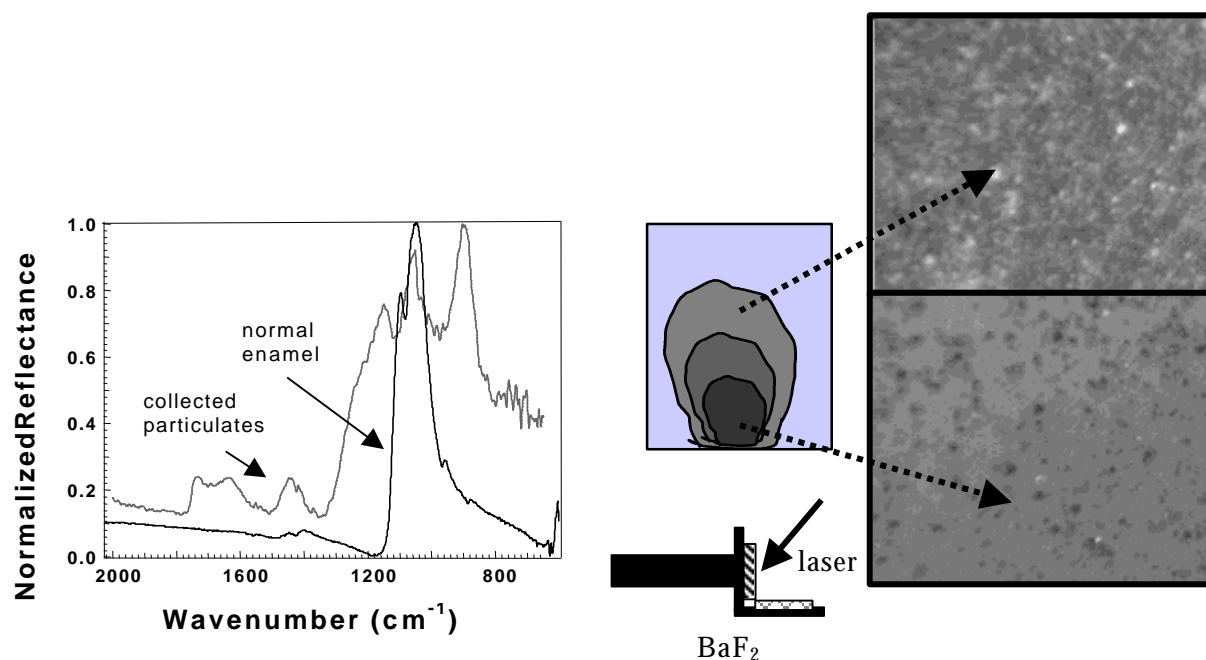
Fig. 1 Spectra of ejected particles collected in vacuum after the laser ablation of enamel using a 9.6 μm TEA CO_2 laser. The particles are deposited in a fan shaped distribution on a BaF_2 substrate. Optical images (320x) of the low density zone (top) and high density zone (bottom) are shown on the right. SR-FTIR spectra of the particles(gray) and normal enamel are shown on the left.

changes associated with the ablation process. The energy deposition and maximum temperature are greatest at the center of crater created by the ablation process and decreases with distance from the crater center. The chemical composition of the crater walls deviated significantly from that of hydroxyapatite after Er:YAG and CO_2 laser irradiation without added water. The high spatial resolution of beam line 1.4.3 allowed identification of the mineral phases present on the crater walls [12, 13] These mineral phases have not been previously reported because of the limited resolution of conventional IR spectroscopy systems.

We postulated that the non-apatite mineral phases originate from the plume of ejected material above the ablated area. In order to confirm that hypothesis, we collected the ablated mineral phases on BaF_2 substrates in vacuum. SR-FTIR spectra were used to show the distribution of phases as a function of distance from the site of laser ablation (Fig. 1). Such data confirms that the mineral phase distribution around the ablation craters is due to recondensation from the plume. We are continuing this effort with other laser wavelengths, energy deposition conditions, and quantities of water to determine the optimum ablation conditions with limited subsurface damage and improved surface conditions for bonding or resistance to environmental degradation. Supported by NIH/NIDCR R29DE12091.

1. Stern R.H.and Sognnaes R.F.: Laser beam effect on hard dental tissues. J. Dent. Res. 43:873, 1964.
2. Wigdor H.A., Walsh J.T., Featherstone J.D.B., Visuri S.R., Fried D.and Waldvogel J.L.: Lasers in Dentistry. Lasers Surg. Med. 16:103-133, 1995.

3.   Altshuler G.B., Belikov A.V., Erofeev A.V.and Skrypnik A.V.: Physical aspects of cavity formation of Er-laser radiation, Lasers in Dentistry, Vol. 2394. 211-222 (SPIE, San Jose, 1995).

4.   Rechmann P., Glodin D.S.and Hennig T.: Changes in surface morphology of enamel after Er:YAG irradiation, Lasers in Dentistry IV, Vol. 3248. 62-68 (SPIE, San Jose, 1998).

5.   Featherstone J.D.B.and Nelson D.G.A.: Laser effects on dental hard tissue. Adv. Dent. Res. 1:21-26, 1987.

6.   Konishi N., Fried D., Featherstone J.D.B.and Staninec M.: Inhibition of secondary caries by CO2 laser treatment. Amer. J. Dent. 12:213-216, 1999.

7.   Fowler B.and Kuroda S.: Changes in heated and in laser-irradiated human tooth enamel and their probable effects on solubility. Calcif. Tissue Int. 38:197-208, 1986.

8.   Constantz P.W.B.a.B.: Hydroxyapatite and Related materials (CRC Press, Boca Raton, 1994).

9.   Elliot J.C.: Structure and Chemistry of the Apatites and other Calcium Orthophosphates (Elsevier, Amsterdam, 1994).

10.   Kuroda S.and Fowler B.O.: Compositional, structural and phase changes in *in vitro* laser-irradiated human tooth enamel. Ca1cif. Tissue Int. 36:361-369, 1984.

11.   Fried D., Murray M.W., Featherstone J.D.B., Akrivou M., Dickenson K.M.and Duhn C.: Dental hard tissue modification and removal using sealed TEA lasers operating at λ=9.6 µm. J. Biomedical Opt. 196-203, 2001.

12.   Ashouri N., Shori R., cheung J.M.and Fried D.: IR Laser Ablation of Dental Enamel: Influence of an Applied Water Layer on Ablation Rate and Peripheral Damage, Lasers in Dentistry VII, Vol. 4249, 72-79 (2001).

13.   Fried D.and Breunig T.M.: Infrared Spectroscopy of Laser-irradiated Dental Hard Tissues using the Advanced light Source, Lasers in Dentistry VII, Vol. 4249, 99-104 (2001).

Principal investigator: Dan Fried, University of California, San Francisco, 415-502-6641, fried@itsa.ucsf.edu.

Investigation of calcifications in breast tissue using EXAFS and XRF

D.E. Sayers[1], M.Z. Kiss[1], A.C. Thompson[2], M. Marcus[3]

[1]Department of Physics, North Carolina State University, Raleigh, North Carolina 27695
[2]Advanced Light Source Division, Ernest Orlando Lawrence Berkeley National Laboratory, University of California, Berkeley, California 94270
[3]Center for X-Ray Optics, Ernest Orlando Lawrence Berkeley National Laboratory, University of California, Berkeley, California 94270

EXAFS studies have recently been conducted on calcifications in breast tissue as part of an ongoing study in the connection of calcifications to breast cancer. It has been determined that the chemical composition of calcifications is related to the development of benign or malignant breast disease [1, 2]. We are interested in improving the understanding of this connection. For our initial experiments, calcifications were removed from non-cancerous breast tissue and scanned using the EXAFS setup on beamline 10.3.2. EXAFS spectra were collected from several regions in the samples and compared to the standard spectra of hydryoxy apatite, calcium oxalate, monetite, and brushite. Figure 1 is an example of our initial results. The XANES spectra from four regions on one sample are compared with hydroxy apatite. It is clear that region A most closely resembles the hydroxy apatite spectrum. The other regions display other features in the spectra that are not present in hydroxy apatite and have not yet been accounted for in the other standards. The presence of other compounds in the calcification is a possibility, though it is not clear what role they play.
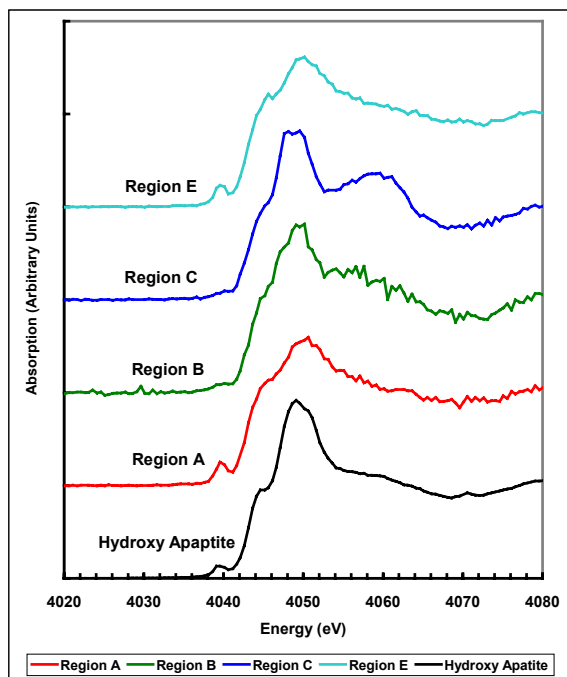

Figure 1. XANES spectra of four regions on a calcification sample from breast tissue, taken at the Ca edge. The four regions are compared to the XANES spectrum of hydroxy apatite

Additionally, XRF studies have been conducted on these tissue samples to investigate the elemental distribution in the calcifications. These studies were run concurrently on beamline 10.3.1. Figure 2 is a photo of one of the samples with the location of the calcification indicated by the dashed lines. Figure 3a is a map of the calcium concentration of this sample. The highest

concentration occurs in the region of the calcification. Other elements were present in the sample, and figure 3b shows the zinc concentration. There is a clear correlation between the calcium and the zinc with the calcium concentration roughly five times that of the zinc. None of the standards studied using EXAFS contained zinc, suggesting that this sample may contain compounds not normally associated with calcifications.
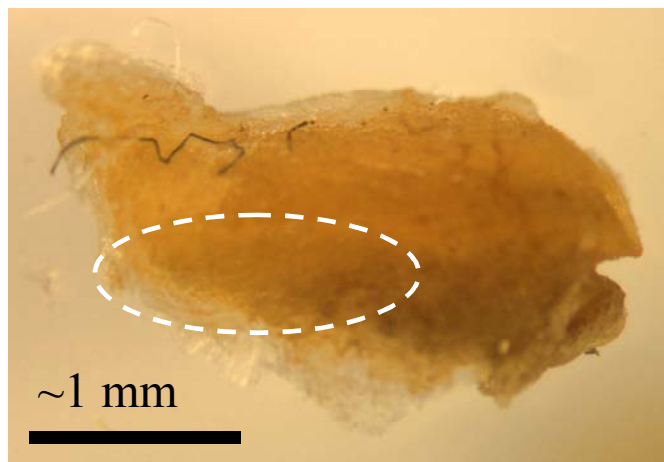

Figure 2. Photograph of one of the tissue samples. The dashed lines enclose the region of the calcification.
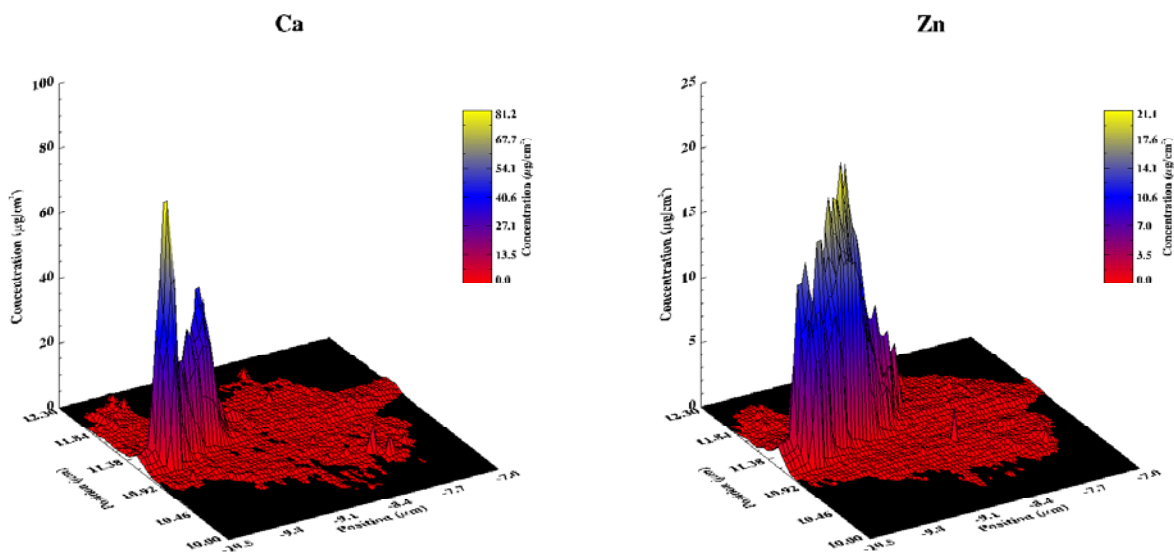
Figure 3. Concentration maps of a) Ca and b) Zn from the sample shown in figure 2.

References:
1.   A. Fandos-Morera, M. Prats-Esteve, J.M. Tura-Soteras, A. Traveria-Cros, Radiology, **169**, 325 (1988).
2.   M.J. Radi, Arch. Pathol. Lab. Med., **113**, 1367 (1989).

Novel molecular mechanisms of disease susceptibility in plants -- an FTIR study of *Arabidopsis thaliana*

Theodore K. Raab[1], John Vogel[2], Shauna Somerville[1]

[1] Carnegie Institution of Washington, Dept. of Plant Biology,
260 Panama Street, Stanford, CA 94305, USA
[2] University of California, Dept. of Plant Pathology,
Riverside, CA 92521, USA

INTRODUCTION

Understanding the molecular basis of plant resistance to fungal diseases will contribute to reducing world-wide crop losses. One model organism for studying disease resistance is *Arabidopsis thaliana*, a small member of the mustard family for which complete genomic sequence information was publicly released in 2000. *Erysiphe cichoracearum*, the causative agent for powdery mildew disease in a wide range of plants, colonizes and eventually overtakes a host if three events occur. *Erysiphe* spores are carried on the wind, and when they land on the aerial portions of a host plant, they must invade an epidermal (outer) cell, and establish a feeding structure to divert plant nutrients. The fungus must "fly under the radar" of the host's defense responses, which would, if fully activated, quickly kill the invading fungus. Finally, since the fungus is not a saprophytic pathogen (cannot survive on dead tissues), it must keep the host's cells alive until its life cycle is complete. Several genetic loci conferring *p*owdery *m*ildew *r*esistance (*pmr*1-4) have previously been described by Vogel and Somerville [1]. While many disease-resistance pathways involve sensing of salicylic acid and/or jasmonic acid, several genes that operate independently of these hypersensitive responses have been identified; the mutant described below represents a novel form of disease resistance based upon loss of a gene required during a compatible interaction, rather than the action of known host defense pathways.

METHODS

An *Arabidopsis* disease-resistance gene named *PMR*6 has recently been cloned and characterized and encodes a pectate lyase-like enzyme with a novel C-terminal domain [2]. Although the protein has been purified, it has resisted all efforts at demonstrating enzymatic activity towards cell wall polysaccharides. Utilizing Beamline 1.4.3, we undertook a comparative FTIR microscopic study of cleared leaves from wild type (WT) Columbia plants of *Arabidopsis*, as well as plants homozygous for a loss-of-function mutation in *pmr*6. We reasoned that large scale modifications in the pectin component of the cell wall in the mutant compared to wild type should be instructive as to the nature of the molecular lesion. IR spectromicrosopy at BL 1.4.3 allows the chemical characterization of distinct cell types in both living and chemically-cleared tissues at a spatial scale of 6 μm x 10 μm, a significant improvement over thermal IR sources. For these experiments, a few dozen matched seedlings of Columbia WT and *pmr*6-1 were germinated on 1.5% agar plates supplemented with 0.5x MS medium, and cultivated in

growth cabinets at 21° C with {16:8} photoperiod. After 2 weeks, the seedlings were transplanted to a peat:perlite mix supplemented with slow-release fertilizer, and grown an additional 10-12 days in a walk-in growth chamber with continuous light. At the early bolting stage, rosette leaves of both treatments were cleared in 1:1 chloroform:methanol and air-dried flat overnight on microscope slides under sterile cover slips. IR spectra were collected (upon removal of the cover slips) in single-beam reflectance mode at 2 cm^{-1} resolution over the range of 4000 - 650 cm^{-1} (2.5 to 16 micron wavelength) with 512 spectra co-added for Fourier transforms. Spectra were then converted to absorbance basis by ratioing to a gold-coated reflection standard, and small amounts of CO_2 and water vapor subtracted from the spectra. At least a dozen (biological replicates) plants from each class were compared.

For initial data exploration, spectra were converted from Nicolet's OMNIC software controlling the microscopes at BL 1.4.3, to the JCAMP.DX format, and analyzed after area-normalization using **Win DAS** [3], a widely used multivariate statistical package in biotechnology and biospectroscopy. For extremely multivariate data sets such as those produced in FTIR or NMR spectroscopy, the very first step in rational data exploration occurs at the level of dimensional reduction. One such method, principal components analysis (PCA, also known as singular-value decomposition) seeks a new set of m axes (<< r, the number of variates in each spectrum) that projects as much of the variance in the original data as possible. Using a covariance matrix, the software initially calculates a ranking (from increasing to decreasing variance) of the top ten vectors that "span" the original data. In most spectral applications, the first two or three PCs explain much of the difference between the 'treatment' and 'control', often highlighting spectral contributions (known as PC 'loadings' or 'scores') hard to see in the original spectra. Below we discuss two of the products of such an analysis to interpret the molecular distinction between wild type *Arabidopsis* plants and those carrying the disease resistance lesion. It should be kept in mind however, that chemometrics methods are quite general, and can be used, e.g. for interpretation of remote sensing data, as well as DNA microarray experiments in clinical medical settings.

RESULTS

To determine if mutations in PMR6 altered cell wall composition, FTIR spectra were acquired at BL 1.4.3. **Figure 1** compares the mean absorbance spectra of a dozen WT leaves (green) and eighteen *pmr6* leaves (blue) in the carbohydrate 'fingerprint' region from 1800-800 cm^{-1}. Visual inspection of the absorbance spectra from *pmr6* leaves reveals somewhat greater absorbance in the region

attributed to pectin, a major class of cell wall polysaccharides in plants. This is not surprising given that *pmr6* may be a pectin-degrading enzyme. The absorbance peaks
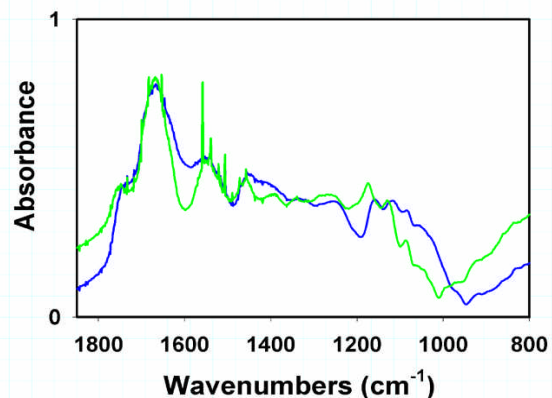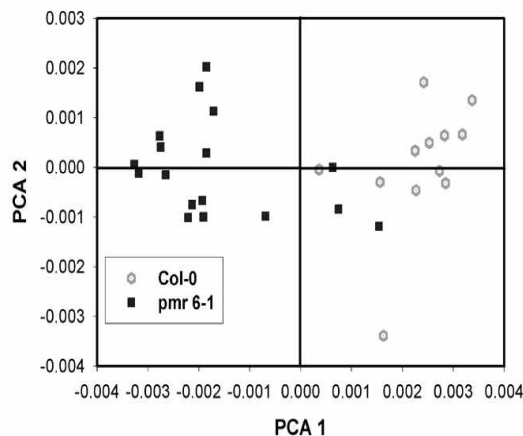
attributed to cellulose in *pmr*6 cell walls shift down in energy, indicating a greater degree of hydrogen-bonding than WT.
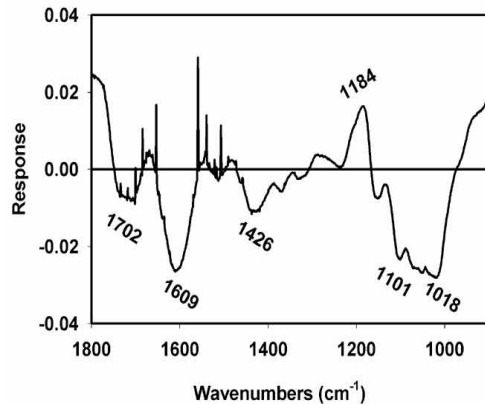
Principal components analysis was employed to identify features that differ between *pmr*6 and wild type, but that are not obvious in the raw spectra. The first three PCs explained 64%, 19% and 9%, respectively of the variation in the full data set. The signature peaks (1609, 1101, 1018 cm^{-1}) of the of the first principal component (**Figure 2A**) points to the enrichment of the of the *pmr*6 cell wall in pectins with a lower degree of esterification and that *pmr*6 cellulose has more intermolecular hydrogen bonds (1426 cm^{-1}) than WT. The 2nd PC (not shown) corresponded to higher levels of protein in the *pmr*6 leaves relative to WT. The statistical separation of the two types of *Arabidopsis* plants

can be seen in the biplot of **Figure 2B**. Spectroscopic observation of the altered pectin composition of the cell wall fits well with the possible pectin-degrading/binding activity for the *PMR6* gene. The alterations of seen by FTIR in *pmr*6 cell wall composition may have made the plants less palatable to the pathogen *Erysiphe* spp. We are at work to identify other actors in this pathway and to interpret changes in cell wall composition by various IR techniques at the ALS.

REFERENCES

1. J. Vogel and S. Somerville, "Isolation and characterization of powdery mildew-resistant *Arabidopsis* mutants," Proc. Natl. Acad. Sci. USA **97**, 1897-1902 (2000).
2. J. Vogel, T.K. Raab, C. Schiff, S. Somerville, "PMR6, a pectate lyase-like gene required for powdery mildew susceptibility in *Arabidopsis*," Plant Cell (in review, 2002).
3. E.K. Kemsley, *Discriminant analysis and class modeling of spectroscopic data.* (John Wiley and Sons, 1998).

Principal Investigator: Dr. Theodore K. Raab, Carnegie Inst. of Washington, Dept. of Plant Biology, 260 Panama St., Stanford CA 94305. Email: tkraab@Andrew2.Stanford.edu. Telephone: 650-325-1521 ext. 446.

Osteoblast-like cell adhesion on bioactive glasses: surface reactions and resistance to trypsinization

S. Foppiano, A.P. Tomsia[1], G.W. Marshall, T. Breunig, D.J. Rowe, and S.J. Marshall

(University of California San Francisco and [1]Lawrence Berkeley National Laboratory Berkeley, CA)

A preliminary study was initiated to identify the early stages of apatite formation on bioactive glass substrates. Several bioactive glasses are being examined to determine the effects of glass composition on the early processes of apatite nucleation and growth. The objective of this project is to improve osseointegration of implant materials for dental and orthopedic applications. The high spatial resolution of the FTIR system on beam line 1.4.3 has allowed us to examine small isolated features on the glass surfaces. We are continuing this effort during the next experimental period by examining the progression of apatite formation with increasing exposure time to simulated body fluid.

We have developed bioactive glass coatings of Ti alloys that provide good metal adhesion while retaining bioactivity. Two of the glasses (6P1 and 6P8) proved to be suitable substrates for the attachment of osteoblast-like cells. Osteoblast-like cells, when seeded on glass 6P8, showed remarkable resistance to detachment by trypsinization. The purpose of this study was to investigate two possible mechanisms underlying trypsin resistance of MG63 osteoblast-like cells on glass 6P8: 1) trypsin inactivation by solubility products released from glass 6P8 in tissue culture medium; 2) differential protein adsorption on the substrates. Glass discs of the same dimensions ($\varnothing = 12$ mm) were finished through 0.05 μm alumina slurry, cleaned by ultra-sonication in alcohol, sterilized in dry heat at 250° C, and placed in 12-well tissue culture plates (N=5 per material). Human osteosarcoma (osteoblast-like) cells (MG63) were cultured in $\alpha-$MEM with 10% fetal calf serum and antibiotics. 4×10^5 cells in a 20 μL aliquot were plated on each glass or titanium alloy (Ti6Al4V), as a control. Cells were allowed to settle for 1 hr prior to flooding with medium. After 30 min cells were treated with 1.5 mL of trypsin, either fresh or previously incubated for 1 hr with a disc of glass 6P8. Cells were completely detached from Ti6Al4V at 5 min and glass 6P1 at 10 min. After 15 min cells were still adhering onto glass 6P8, as previously observed. Therefore, cell adherence does not seem to be due to glass 6P8 reactivity products inactivating trypsin. Then specimens of the same two glasses and Ti6Al4V (control) (N=4) were prepared, as described above, and incubated with 2 mL of fetal calf serum for 2 hr at 37 °C. Samples were gently rinsed with PBS to remove weakly adsorbed proteins and desorbed with 10 rinses of 500 μL of 0.1% sodium dodecyl sulphate (SDS). The SDS rinses were collected and analyzed for protein concentration, using a spectrophotometric assay (BioRad Laboratories, and Molecular Devices ν max kinetic microplate reader) with serum albumin as the standard. Data normalized to sample surface area showed significant differences in the amount of protein adsorbed per unit of surface area among substrates (6P8>6P1>Ti6Al4V, one-way ANOVA p<0.001). Aliquots of the same samples were fractionated by SDS-polyacrylamide gel electrophoresis, and the proteins visualized by staining with Coomassie blue. The distribution of the bands indicated differential protein adsorption between the bioactive glasses and Ti6Al4V. Glass surfaces were analyzed by Fourier transform infrared spectroscopy (FTIR) before and after the protein adsorption

experiments to identify surface reactions and residual adsorbed proteins. FTIR surface analysis showed that glass 6P8 readily reacted in solution, forming silanols, while glass 6P1 did not. These results indicate that resistance to trypsinization of osteoblast-like cells from glass 6P8 may be due to differential protein adsorption but not to trypsin inactivation. Supported by NIH/NIDCR Grant DE 11289

Principal investigator: S. Foppiano, University of California, San Francisco, (415) 476-2048

Synchrotron Infrared Spectromicroscopy as a Novel Bioanalytical Microprobe for Individual Living Cells: Cytotoxicity Considerations

Hoi-Ying N. Holman,[*] Kathleen A. Bjornstad,[†] Morgan P. McNamara,[†]
Michael C. Martin,[‡] Wayne R. McKinney,[‡] and Eleanor A. Blakely[†]
[*]Center for Environmental Biotechnology, [†]Life Sciences Division, [‡]Advanced Light Source Division,
Lawrence Berkeley National Lab, Berkeley, CA, 94720

INTRODUCTION

Recent progress in analytical instrumentation has enabled dramatic advances in gene sequencing and protein identification techniques. Using the information produced by these techniques, the attention of biomedical researchers is now increasingly focused on understanding how chemical species interact in living organisms by the use of imaging techniques that simultaneously provide morphological and chemical information within cells and tissues. Most imaging research has focused on fluorescent labeling to locate a specific chemical event within the cell. However, bond breaking, ionization, and other damage has been shown to occur during excitation with UV, visible, and even the more recent near-IR two-photon techniques.

In contrast, synchrotron-based Fourier transform infrared (SR-FTIR) spectromicroscopy has the ability to monitor the chemistry within an individual living cell without labels and with even lower photon energies. Combining SR-FTIR spectroscopy with microscopy yields a powerful tool for non-destructively probing bio-systems on a small size scale. The sample can be small and/or heterogeneous, for example; individual living cells, microorganisms, and larger biological systems in which local biochemistry may have significant spatial variations.

It is crucial to know if the synchrotron radiation-based mid-infrared (SR-IR) source causes any short- or long-term effects on the living biological samples under study. Mid-infrared photons are significantly lower in energy ($0.05 – 0.5$ eV) than excitation sources used for fluorescence, implying that photo-induced effects will be minimal. However, to be assured that the SR-IR beam does not perturb living samples via other mechanisms, more detailed studies are required. We recently measured that sample heating from the synchrotron IR beam is minimal (~ 0.5°C).

Here we present the results of in vitro studies to determine if the SR-IR beam causes any detectable immediate or long-term cytotoxic effects on living cells. Four widely accepted assays were used to look for deleterious effects on cells subjected to the SR-IR beam.

MATERIALS AND METHODS

The studies used a human T-1 cell-line from an established aneuploid cell-line derived from human kidney tissue. They were maintained in a standard growth medium at pH 7.4. Cells were grown at 37°C in a humidified atmosphere of 5% CO_2 and 95% air. Cells were sub-cultured every 3-4 days. T-1 cultures were grown to confluence to ensure para-synchronization. Fluorescence-activated Cell Sorting (FACS) analysis demonstrated that 85% of the cells in these cultures were synchronized to G0/G1 phases. A custom on-stage mini-incubator was used to maintain the proper moisture and growth environment for the cells while allowing *in situ* FTIR spectromicroscopy measurements. Selected cells were exposed at 37°C to the focused synchrotron infrared beam for a specified duration of 5, 10, or 20 minutes. Once completed, fresh growth media was replaced on the dish and it was returned to the standard incubator.
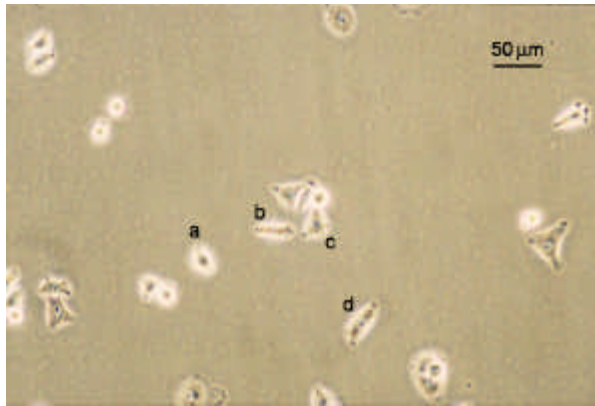
Figure 1. Photograph showing results from alcian blue assays of cells exposed to the SR-IR beam for (a) 5, (b and c) 10, and (d) 20 minutes. Other cells were not exposed and were negative controls. No cells show retention of the blue dye demonstrating that no immediate cytotoxicity is observed.

Negative controls were non-exposed cells located in the same field (internal controls), and therefore experienced the same handling. Positive controls were cells killed by either a 70% alcohol solution or dehydration.

RESULTS AND DISCUSSION

Figures 1-4 show representative photographs for each assay. In no case did we find a result differing with the representative ones shown.

SR-IR beam has no short-term effect on cell viability. Alcian blue assays were carried out as shown in Figure 1. Neither cells exposed to up to 20 minutes of synchrotron IR beam nor nearby non-exposed cells retained the blue dye 6 hours after exposure. This indicates that the SR-IR beam did not produce detectable effects on the viability of exposed cells. Other exposed cells remained free of stain 12 and 24 hours after exposure indicating that their membranes still remained intact. In contrast, dead positive control cells were stained blue as expected, as their membranes had become permeable to the dye molecules.

Cells survive and continue to proliferate days post exposure. The long-term colony-forming assay demonstrates that the exposed cells also continue to proliferate into colonies. The exposed test cells and nearby non-exposed cells proliferated into colonies of similar size (Figure 2), well over fifty cells in ten days. The positive control cells, on the contrary, had detached from the petri dish and disappeared from the field. Since none of the 46 SR-IR exposed test cells developed into colonies with less than 50 cells, we interpret this as an indication that SR-IR beam does not impact cell survival and proliferative activities.

Exposure to SR-IR does not compromise cell-cycle progression. Cell-cycle progression in exposed cells were monitored by the incorporation of BrdU into newly synthesized DNA at 11 hours after cell setup and 10 hours post SR-IR exposure. Both exposed cells and non-exposed controls had reached the DNA synthetic phase (S-phase) of cell- cycle at this 12-hour observation point (Figure 3). The similarities among these immunofluorescent staining of BrdU (and DAPI) labeled cells indicate that the exposed cells are not compromised in their ability to enter their S-phase in the cell cycle after exposure to the SR-IR beam. Furthermore, the lack of BrdU uptake in exposed and control cells at 6 or 24 hours demonstrates that the cell-cycle
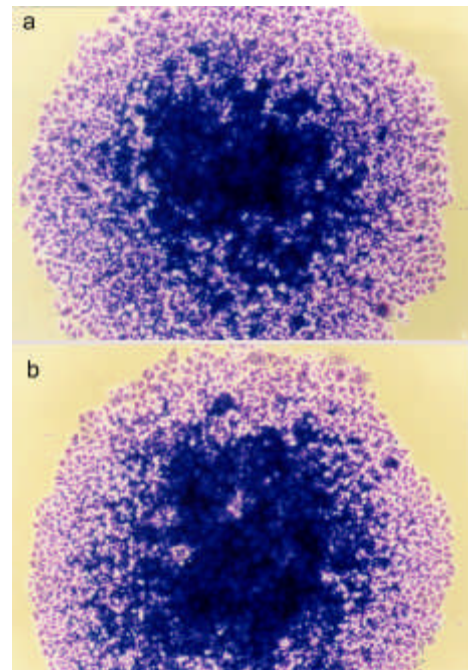

Figure 2. Colony forming from (a) a negative control cell and (b) a test cell exposed to the SR-IR beam for 20 minutes. Both cells proliferated into similar sized colonies after 10 days.
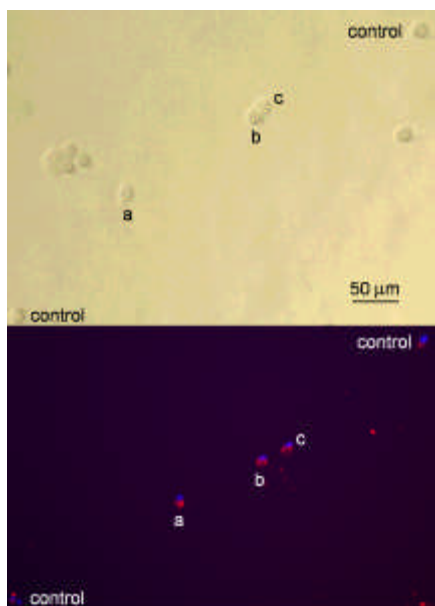
Figure 3. BrdU assay results for cells exposed to the SR-IR beam for (a) 5, (b) 10, and (c) 20 minutes. Two other cells in the field were unexposed and used as negative controls. In the lower panel, blue indicates DNA and red indicates BrdU incorporation during DNA synthesis. All cells show the same incorporation of BrdU into the DNA.
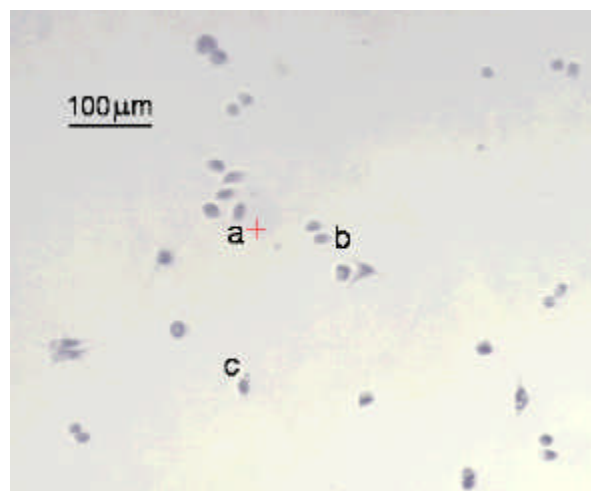

Figure 4. MTT assay results for cells that had been exposed to the SR-IR beam for (a) 5, (b) 10, and (c) 20 minutes. Other cells in the field were unexposed and used as controls. All test and control cells show the same blue color indicating the same level of metabolic activity.

progression of SR-IR exposed cells remains uninterrupted.

ATP and NAD+-associated metabolic activity is not impaired by the SR-IR beam. A two-hour MTT assay was carried out and representative photos of the results are shown in Figure 4. Cells exposed for 20 minutes and nearby non-exposed controls show similar purple-blue stain. On the contrary, tetrazolium salt solution remained yellow in the killed (positive) controls with no purple-blue stain uptake. Results were identical for 5- and 10-minute exposures. This implies that both the exposed and negative control cells produced mitochondrial dehydrogenases during the two-hour MTT assay. Mitochondrial dehydrogenases are associated with the ubiquitous metabolic pathway of glycolysis that generates the critical biomolecules of ATP and NAD+. These results indicate that the SR-IR beam has negligible effects on this important metabolic pathway which provides energy to cells.

In all 4 assays studied we found no detectable changes between cells exposed to the synchrotron infrared beam and nearby non-exposed controls. 267 individual cells were tested with zero showing measurable cytotoxic effects (counting statistics error is 6.1%), with over 1000 control cells used. These results show that the high-brightness mid-IR synchrotron beam is not only non-destructive, but also causes no effects on both the short- and long-term viability, proliferation, and metabolism within living human cells. The results reported here lay an important foundation for future biomedical and biological applications of synchrotron infrared spectromicroscopy, which will complement other biochemistry and microscopy techniques.

Principal investigator: Hoi-Ying N. Holman, Lawrence Berkeley National Laboratory. Email: hyholman@lbl.gov. Telephone: 510-486-5943.